

Electronic structure and thermodynamic stability of LaMnO_3 and $\text{La}_{1-x}\text{Sr}_x\text{MnO}_3$ (001) surfaces: *Ab initio* calculations

Sergei Piskunov,^{1,2,*} Eugene Heifets,³ Timo Jacob,⁴ Eugene A. Kotomin,^{2,3} Donald E. Ellis,⁵ and Eckhard Spohr¹

¹Department of Theoretical Chemistry, University of Duisburg-Essen, Universitätsstrasse 2, D-45141 Essen, Germany

²Institute for Solid State Physics, University of Latvia, 8 Kengaraga Street, Riga LV-1063, Latvia

³Max-Planck-Institute for Solid State Research, Heisenbergstrasse 1, D-70569 Stuttgart, Germany

⁴Department of Electrochemistry, Ulm University, D-89069 Ulm, Germany

⁵Department of Physics and Astronomy, Northwestern University, Evanston, Illinois 60208-3108, USA

(Received 13 August 2008; published 24 September 2008)

We present the results of *ab initio* hybrid density-functional calculations of the atomic and the electronic structures of LaMnO_3 (LMO) and $\text{La}_{1-x_b}\text{Sr}_{x_b}\text{MnO}_3$ (001) surfaces. The total energies obtained from these calculations were used to analyze thermodynamic stability of the surfaces. We predict Sr and O vacancy segregation to the surface to occur with similar energies (~ 0.5 eV per defect). In pure LMO only MnO_2 termination is thermodynamically favorable under typical operational conditions of a cathode in solid oxide fuel cells, whereas Sr doping makes $\text{La}(\text{Sr})\text{O}$ termination favorable. Finally, the role of Sr doping in cathode degradation is discussed.

DOI: 10.1103/PhysRevB.78.121406

PACS number(s): 73.20.At, 71.15.Mb

Due to their outstanding magnetic and electrical properties, such as colossal magnetoresistance, half-metallic behavior, and composition-dependent metal-insulator transition,^{1,2} LaMnO_3 (LMO) and $\text{La}_{1-x_b}\text{Sr}_{x_b}\text{MnO}_3$ (LSM) perovskite-type oxides continue to attract considerable attention. Furthermore, due to its high electrochemical performance, thermal and chemical stability, and compatibility with yttria-stabilized zirconia (YSZ) electrolyte, LSM ($x_b \sim 0.2$) has been actively used as a mixed ionic-electronic conducting electrode in high-temperature solid oxide fuel cells (SOFCs).³

For better understanding of the mechanism of oxygen reduction at the LSM nanothin cathode deposited on a YSZ electrolyte, a detailed study of LSM surface properties at the atomistic level is of high importance. To date, a few *ab initio* studies on both LMO (Refs. 4 and 5 and references therein) and LSM (Refs. 6 and 7) surfaces have been performed. However, to the best of our knowledge, the only thermodynamic analysis of manganite surface stability⁸ was focused on pure LMO, while the analysis of LSM solid solutions⁹ considered its bulk properties. No theoretical studies so far have dealt with Sr-dopant effects on LSM surface properties.

In this study, we apply the *ab initio* thermodynamics approach, which was developed earlier for two- and three-component systems,^{10–12} in order to analyze stability of a four-component LSM (001) surfaces under SOFC operation temperatures (up to 900 °C) and realistic oxygen gas pressures. Using *ab initio* computations we determined surface electronic and atomic structures of both pure and Sr-doped LMO. Then the obtained total energies were used in the thermodynamic analysis of surface stability. The following structures were studied: (i) $\text{La}(\text{Sr})\text{O}$ - and MnO_2 -terminated (001) surfaces of cubic LMO and LSM [Figs. 1(a) and 1(c)]. Both LMO and LSM exhibit (pseudo)cubic structures at elevated temperatures³ which are of our interest here. Although LSM thin films are polycrystalline, the (001) surface has the lowest energy in both LMO (Ref. 4) and LSM (Ref. 5) and we restrict our consideration here to this surface: (ii) $\text{La}(\text{Sr})\text{O}$ - and MnO_2 -terminated (001) surfaces of cubic LSM contain-

ing surface oxygen vacancies [Figs. 1(b) and 1(d)], which are responsible for LSM ionic conductivity; and ³ (iii) $\text{La}(\text{Sr})\text{O}$ -terminated (001) surfaces with enrichment of Sr at the surface [Figs. 1(e)–1(g)]. Sr segregation is observed in LSM thin films (see Ref. 13 and references therein) which can decrease the cathode performance.¹⁴

In our *ab initio* calculations we use DFT-HF (*i.e.*, density functional theory and Hartree-Fock) hybrid exchange-correlation functionals which gave very good results for the electronic structure in our previous studies of both LMO and LSM.^{4,15} We employ here the hybrid B3LYP exchange-correlation functional.¹⁶ The simulations were carried out with the CRYSTAL06 computer code,¹⁷ employing atom-centered Gaussian-type functions as a basis set (BS). The computational details are discussed in Ref. 15. For La we have employed the extended BS with an additional *f*-type orbital. Reciprocal space integration was performed by sampling the Brillouin zone with the 4×4 Monkhorst-Pack mesh.¹⁸ To cancel the macroscopic dipole moment perpendicular to a polar (001) surface, we used symmetrical nine-layer slabs terminated on both sides the same way [MnO_2 or $\text{La}(\text{Sr})\text{MnO}$] (see Fig. 1). In our simulations all atoms have been allowed to relax freely. This approach was initially tested on bulk properties,¹⁵ where it very well reproduced the experimentally measured atomic, electronic, and low-temperature magnetic structure of pure LMO and LSM ($x_b = 1/8$). Analysis of surface relaxation showed a considerable rumpling compared to the bulk-truncated surface structure (approximately 2.5% of a_0): O ions of the MnO_2 -terminated surface strongly move inward (0.13 Å) toward the slab center, while surface Mn ions only show a slight displacement (0.03 Å). The Mulliken effective charges in the LMO bulk indicate a considerable covalency contribution to the Mn-O chemical bonding.⁴ On the MnO_2 -terminated surfaces both O and Mn ions become additionally more positive by $0.15e$ and $0.03e$, respectively. The effect of an increased Ti-O bond covalency near the SrTiO_3 surfaces was also recently observed.¹¹ Introduction of Sr ions substituting for La ions in the second plane produces a strong local perturbation. As a

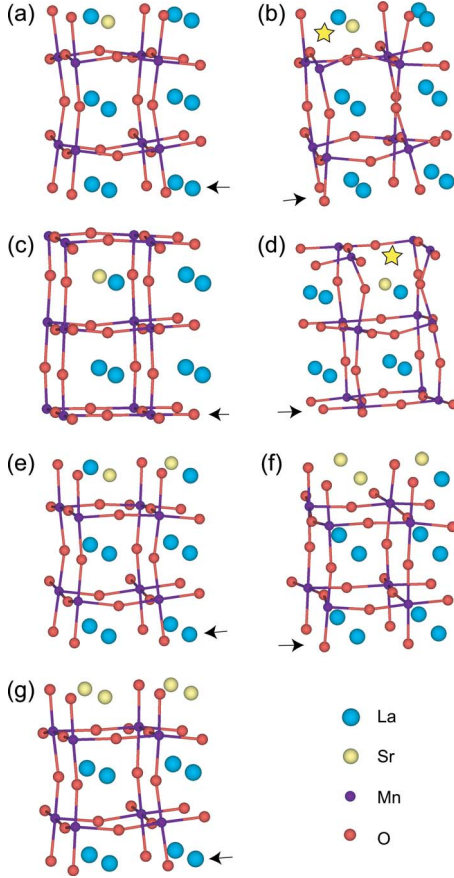


FIG. 1. (Color online) The schematic representation of calculated equilibrium geometries of LSM (001) structures: (a) La(Sr)O termination ($x_s=1/4$), (b) the same as (a) but containing an oxygen vacancy, (c) MnO₂ termination ($x_s=1/4$), (d) the same as (c) but containing an oxygen vacancy, (e) La(Sr)O termination having $x_s=1/2$, (f) the same as (e) but $x_s=3/4$, (g) the same as (e) but $x_s=1$ (full SrO layer). Yellow (gray) stars depict the positions of removed oxygen atoms. Arrows point out a mirror plane of symmetrically terminated slab unit cells.

result some O ions strongly move inward (up to 0.21 Å), while others go outward (up to 0.33 Å); Mn ions relax inward (0.16 Å). This is accompanied by local charge redistribution: some O ions get additional positive charge up to 0.35e, with Mn ions up to 0.08e. The density of states (DOS) calculated for the orthorhombic LMO surfaces of both terminations reveals half-metallic A-type antiferromagnetic (A-AFM) ground states (*i.e.*, Mn spins are parallel in basal plane and antiparallel from plane to plane), with the gaps in minority spins of 1.5 and 2.2 eV for MnO₂- and LaO-terminated surfaces, respectively. The cubic LSM surface reveals a conducting A-AFM state, which is in line with experimental data.¹⁹ A comparison of the slab total energies for Sr on the surface and third layer gives an estimate for the Sr segregation energy of 0.54 eV per Sr ion. This could be compared with the 0.16 eV estimated from experimental data in Ref. 13. The discrepancy could be ascribed to the difference in Sr concentrations, terminations (SrO in our case, MnO₂ in experiments), gas pressure, and temperature.

The stable crystalline surface has to be in equilibrium

with both LSM bulk (with concentration of Sr atoms $x_b=1/8$) and surrounding O₂ atmosphere while an exchange of atoms between the surface and environment is allowed. Therefore, the most stable surface has the lowest Gibbs free surface energy. For the LSM surfaces this can be derived similarly to Refs. 10–12,

$$\Omega_t(x_b, T, p) = \frac{1}{2A} \left[\phi_t(x_b) - \left(N_{\text{Mn}} - \frac{1}{x_b} N_{\text{Sr}} \right) \Delta\mu_{\text{Mn}} - \left(N_{\text{La}} - \frac{1-x_b}{x_b} N_{\text{Sr}} \right) \Delta\mu_{\text{La}} - \left(N_{\text{O}} - \frac{3}{x_b} N_{\text{Sr}} \right) \Delta\mu_{\text{O}}(T, p) \right], \quad (1)$$

where t indicates the surface terminations, A the unit cell surface area, and N_i the number of atoms of type i in the slab unit cell. $\Delta\mu_i = \mu_i - E^i$ ($i = \text{La, Mn}$) are deviations of chemical potentials for metal atoms from their energy in the bulk metals. For the oxygen atom such a deviation is considered with respect to the energy of an oxygen atom in the ground triplet state of an O₂ molecule $\Delta\mu_{\text{O}} = \mu_{\text{O}} - \frac{1}{2} E^{\text{O}_2}$. The constants ϕ_t for each considered termination t are defined as

$$\phi_t(x_b) = E_t^{\text{slab}} - N_{\text{Sr}} E^{\text{LSM}} - \left(N_{\text{Mn}} - \frac{1}{x_b} N_{\text{Sr}} \right) E^{\text{Mn}} - \left(N_{\text{La}} - \frac{1-x_b}{x_b} N_{\text{Sr}} \right) E^{\text{La}} - \left(N_{\text{O}} - \frac{3}{x_b} N_{\text{Sr}} \right) \frac{E^{\text{O}_2}}{2}, \quad (2)$$

where E_t^{slab} is the total energy of a slab with surface termination t and E^{LSM} is the LSM total energy averaged per five-atom perovskite unit cell. Because the pV term (V is unit cell volume) and the differences in vibrational Gibbs free energy between the bulk solid and a corresponding slab are negligibly small,¹⁰ we omit these two contributions. This permits replacing the Gibbs free energies in Eqs. (1) and (2) and in the following formulas with the total energies obtained from *ab initio* calculations.

Preventing metal atoms from leaving the LSM crystal requires that their chemical potentials are smaller in LSM than in the bulk metals (La, Mn, and Sr),

$$0 > \Delta\mu_{\text{La}}, \quad 0 > \Delta\mu_{\text{Mn}}, \quad (3)$$

$$0 > \Delta\mu_{\text{Sr}} = (1-x_b)\Delta\mu_{\text{La}} + \Delta\mu_{\text{Mn}} + 3\Delta\mu_{\text{O}}, \quad (4)$$

and in relevant oxides (La₂O₃, Mn₂O₃, and SrO),

$$E_{\text{La}_2\text{O}_3}^f > 2\Delta\mu_{\text{La}} + 3\Delta\mu_{\text{O}}, \quad E_{\text{Mn}_2\text{O}_3}^f > 2\Delta\mu_{\text{Mn}} + 3\Delta\mu_{\text{O}},$$

$$E_{\text{LSM}}^f - x_b E_{\text{SrO}}^f < (1-x_b)\Delta\mu_{\text{La}} + \Delta\mu_{\text{Mn}} + (3-x_b)\Delta\mu_{\text{O}}, \quad (5)$$

as well as in perovskites (LaMnO₃ and SrMnO₃),

TABLE I. Formation energies per formula unit used in analysis of surface stability. Experimental values are from 20.

Material	E^f (eV)	Expt. E^f (eV)
La ₂ O ₃	-19.57	-18.64
Mn ₂ O ₃	-10.55	-9.96
SrO	-7.12	-6.11
LaMnO ₃	-15.56	-14.77
SrMnO ₃	-11.64	
LSM ($x_b = \frac{1}{8}$)	-15.27	

$$\frac{1}{1-x_b} E_{\text{LSM}}^f - \frac{x_b}{1-x_b} E_{\text{SrMnO}_3}^f < \Delta\mu_{\text{La}} + \Delta\mu_{\text{Mn}} + 3\Delta\mu_{\text{O}} < E_{\text{LaMnO}_3}^f, \quad (6)$$

where E_m^f is the formation energy of material m , as shown in Table I.

We evaluate the oxygen chemical potential $\Delta\mu_{\text{O}}(p, T)$ as a function of partial gas pressure and temperature using the standard experimental thermodynamical tables²⁰ as was done in Refs. 10–12. Based on the results of our *ab initio* computations, the diagrams are drawn, showing where different LMO (001) surfaces are stable (Fig. 2). This occurs in the range of the chemical potentials between La₂O₃ and Mn₂O₃ precipitation lines in this figure, whereas outside these lines the crystal decomposes into corresponding oxides. From this diagram one can see that only the MnO₂-terminated surface can be stable at ambient oxygen partial pressure ($p = 0.2$ atm) below the operational temperatures of SOFC, $T \approx 1200$ K. The LaO-terminated surface at the same pressure becomes dominant only above $T \approx 1900$ K; both terminations may appear stable in between these two temperatures.

We have drawn a similar series of surface phase diagram sections for LSM with $x_b = 1/8$ (Fig. 3) and considered

MnO₂-terminated and La_{1-x_s}Sr_{x_s}O-terminated ($x_s = 0.25, 0.5, 0.75, 1.0$) (001) surfaces. These sections show the stability regions for different surfaces at $p = 0.2$ atm and three key temperatures: at room temperature (RT) (300 K), at SOFC operational temperature (1100 K), and at typical sintering temperature (1500 K). The phase diagram indicates that the LSM crystal is stable only within small quadrangle regions in these sections. At RT both considered terminations—MnO₂ and La_{0.75}Sr_{0.25}O—are stable. At the SOFC operational temperature and at higher temperatures only the La_{0.75}Sr_{0.25}O-terminated surface remains stable. Thus, dopant Sr atoms in LSM cause relative stabilization of La_{1-x_s}Sr_{x_s}O-terminated surface with respect to MnO₂-terminated surface. However, if the former surface, as a result of segregation, would contain Sr concentrations of 0.5 monolayer and above, this becomes unstable.

As Fig. 3 shows, with increasing temperatures the MnO₂-surface diagram moves from the stability region through the Mn₂O₃ precipitation line, i.e., Mn₂O₃ nanocrystals are expected to grow at the surface leaving the La_{1-x_s}Sr_{x_s}O-terminated surface behind. This is consistent with observations in Ref. 21. A similar degradation process without Sr requires stronger overheating or very strongly reducing conditions. A further account for oxygen atom adsorption is still necessary. There are indications that the MnO₂-terminated surfaces can be stabilized by adsorbed oxygen atoms,⁸ leading simultaneously to an increase in cathode catalytic activity and to decrease in the rate of cathode degradation.

O vacancy formation energies calculated with respect to the energy of an oxygen atom in an O₂ molecule are 2.7 eV in LSM bulk and 2.2 eV on the MnO₂-terminated surface. That is, the segregation energy to the surface could be estimated as 0.5 eV. Using the oxygen chemical-potential dependence from Fig. 2 and the approach described in Refs. 22 and 23, it could also be estimated that under SOFC operational conditions the formation energies are drastically reduced down to ~ 1 eV for the LSM bulk and to ~ 0.6 eV for the

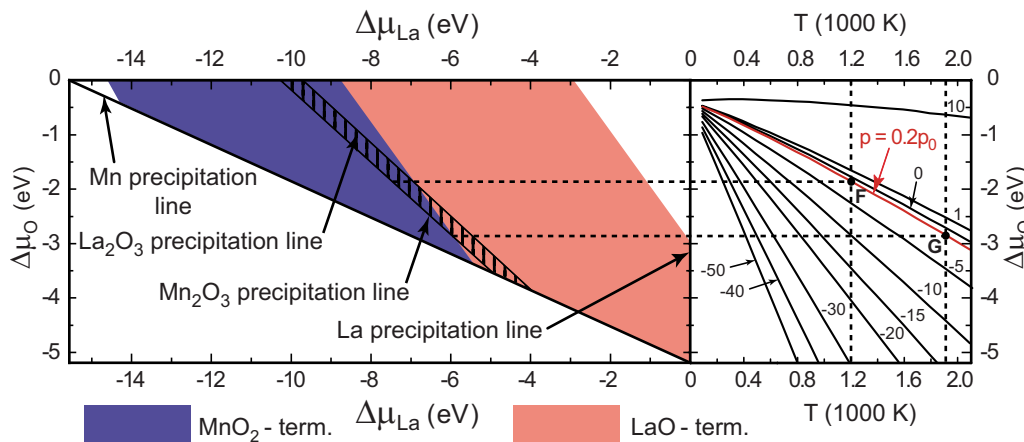


FIG. 2. (Color online) Thermodynamic stability diagram as a function of O and La chemical potentials built for LaMnO₃(001) surfaces. It contains comparison of stability of both LaO- and MnO₂-terminated (001) surfaces and accounts for precipitation conditions for La and Mn metals and their trivalent oxides (La₂O₃ and Mn₂O₃). Stable region is shown as hatched area between La₂O₃ and Mn₂O₃ precipitation lines. The right side shows a family of oxygen chemical potentials under different conditions. The label m indicates the O₂ gas partial pressure: 10^m atm. Red (gray) line corresponds to oxygen partial pressure $p = 0.2p_0$ as in the ambient atmosphere.

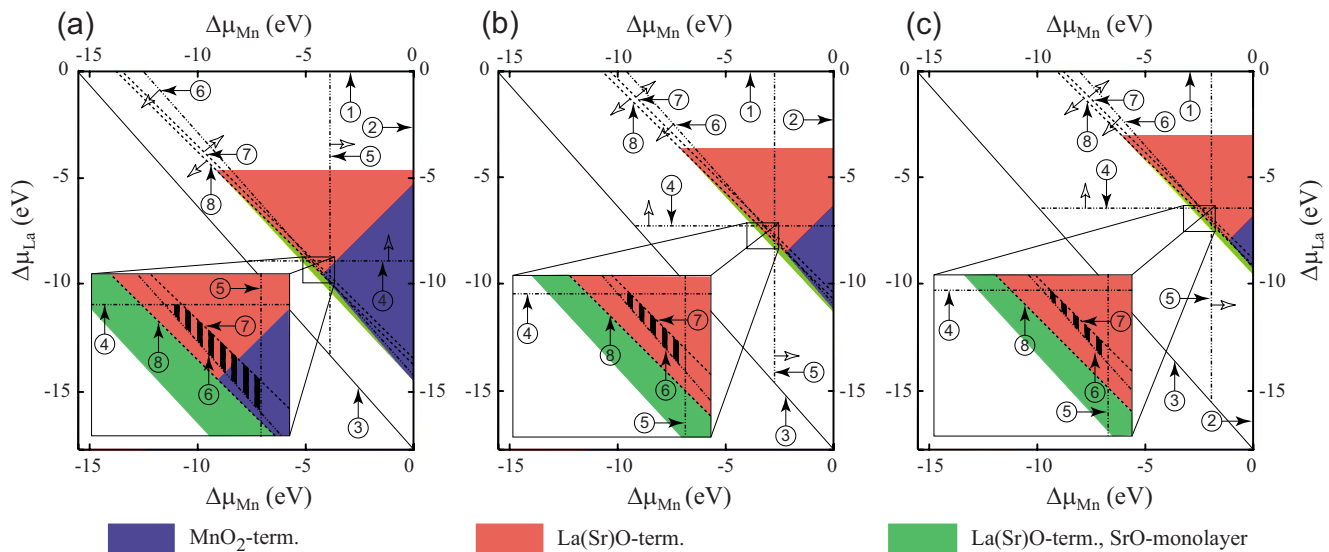


FIG. 3. (Color online) Sections of thermodynamic stability diagram for LSM (001) surface structures (see Fig. 1) for O_2 partial pressure $p=0.2p_0$ and temperatures of (a) 300 K (RT), (b) 1100 K (SOFC operational temperature), and (c) 1500 K (sintering temperature). The region, where LSM ($x_b = \frac{1}{8}$) is stable, is the hatched area between $LaMnO_3$, La_2O_3 , Mn_2O_3 , and SrO precipitation lines. The numbers from 1 to 8 in the circles indicate precipitation lines for (1) La, (2) Mn, (3) Sr, (4) La_2O_3 , (5) Mn_2O_3 , (6) SrO , (7) $LaMnO_3$, and (8) $SrMnO_3$. Hollow arrows indicate the sides from respective precipitation lines where the precipitation occurs. Insets show magnified areas with the region of LSM stability (a hatched quadrangle).

MnO_2 -terminated surface. The neutral oxygen vacancy traps only $\sim 0.6e$ and $\sim 0.2e$ on La(Sr)O- and MnO_2 -terminated LSM (001), respectively. Thus, it is positively charged, makes surrounding atoms strongly polarized, and can serve as potential adsorption centers at LSM surfaces. This will be discussed in detail in a forthcoming paper.

In conclusion, Sr doping in LSM cathodes of SOFC makes the (La,Sr)O-terminated surfaces stable at RT along with MnO_2 -terminated surfaces and the energetically favored surface at SOFC operational temperatures. This opens the way for MnO_2 segregation, poisoning of the surfaces, and finally reduction in the cathode catalytic performance. Our calculations support the experimental data on Sr atom segregation toward the LSM surface and predict a similar process for O vacancies. Significant decrease in the O vacancy for-

mation energy at rising temperatures allows sufficient vacancy concentration to permit efficient work of SOFCs.

This work was supported by the Alexander von Humboldt Foundation, the ‘‘Fonds der Chemischen Industrie’’ (VCI), the MRSEC program of the NSF (Grant No. DMR-0520513) at the Materials Research Center of Northwestern University, the European Social Fund (ESF), and the Latvian Research Programme on Functional Materials and Technologies for Microelectronics and Photonics (Project No. 05.0005.1.1). Computational time by the John von Neumann Institute for Computing (VSR Project No. JIWW31) is gratefully acknowledged. The authors are indebted to J. Maier, J. Fleig, R. Merkle, and Y. Mastrikov for many stimulating discussions.

*sergej.piskunov@uni-due.de

- ¹J. M. D. Coey *et al.*, *Adv. Phys.* **48**, 167 (1999).
- ²A. Haghiri-Gosnet and J. Renard, *J. Phys. D* **36**, R127 (2003).
- ³J. Fleig *et al.*, in *Handbook of Advanced Ceramics: Processing and Their Applications, Vol. II*, edited by S. Somiya *et al.* (Elsevier, Amsterdam, 2003), pp. 59–105.
- ⁴R. A. Evarestov *et al.*, *Phys. Rev. B* **72**, 214411 (2005).
- ⁵Y. Choi *et al.*, *Chem. Mater.* **19**, 1690 (2007).
- ⁶H. Zenia *et al.*, *Phys. Rev. B* **71**, 024416 (2005).
- ⁷Y. Choi *et al.*, *Angew. Chem., Int. Ed.* **46**, 7214 (2007).
- ⁸E. A. Kotomin *et al.*, *Phys. Chem. Chem. Phys.* **10**, 4644 (2008).
- ⁹D. Fuks *et al.*, *Solid State Ionics* **177**, 217 (2006).
- ¹⁰K. Reuter and M. Scheffler, *Phys. Rev. B* **65**, 035406 (2001).
- ¹¹E. Heifets *et al.*, *Phys. Rev. B* **75**, 115417 (2007).
- ¹²K. Johnston *et al.*, *Phys. Rev. B* **70**, 085415 (2004).
- ¹³R. Herger *et al.*, *Phys. Rev. B* **77**, 085401 (2008).
- ¹⁴A. A. Vance and S. McIntosh, *J. Electrochem. Soc.* **155**, B1 (2008).
- ¹⁵S. Piskunov *et al.*, *Phys. Rev. B* **76**, 012410 (2007).
- ¹⁶A. D. Becke, *J. Chem. Phys.* **98**, 1372 (1993).
- ¹⁷R. Dovesi *et al.*, *CRYSTAL06 User's Manual* (University of Torino, Torino, 2006), <http://www.crystal.unito.it/>
- ¹⁸H. J. Monkhorst and J. D. Pack, *Phys. Rev. B* **13**, 5188 (1976).
- ¹⁹K. Horiba *et al.*, *J. Electron Spectrosc. Relat. Phenom.* **144-147**, 557 (2005).
- ²⁰M. W. Chase, *NIST-JANAF Thermochemical Tables* (American Chemical Society, Washington, DC, 1998).
- ²¹J. H. Kuo *et al.*, *J. Solid State Chem.* **83**, 52 (1989).
- ²²S. B. Zhang and J. E. Northrup, *Phys. Rev. Lett.* **67**, 2339 (1991).
- ²³C. G. Van de Walle and J. Neugebauer, *J. Appl. Phys.* **95**, 3851 (2004).